Revisiting the Taylor-Culick approximation: Retraction of an axisymmetric filament

Jean-Lou Pierson, Jacques Magnaudet, Edson Soares, Stéphane Popinet

HAL Id: hal-02747137

https://hal.science/hal-02747137

Submitted on 3 Jun 2020

Revisiting the Taylor-Culick approximation. Part 1: retraction of an axisymmetric filament

Jean-Lou Pierson

*IFP Energies Nouvelles, 69360 Solaize, France**

Jacques Magnaudet

Institut de Mécanique des Fluides de Toulouse (IMFT),
Université de Toulouse, CNRS, Toulouse, France

Edson José Soares

Dpt. Engenharia Mecanica, Univ. Fed. Espirito Santo (UFES), Vitoria, CEP 29075-910, Brazil

Stéphane Popinet

Institut Jean Le Rond D'Alembert, Sorbonne Université, CNRS, 75005 Paris, France

ABSTRACT

We numerically study the retraction of an axisymmetric viscous filament in a passive surrounding fluid. The analysis focuses on the evolution of the tip velocity, from the early stage of the filament retraction until it reaches its final equilibrium spherical shape. The problem is governed by two control parameters: the Ohnesorge number, Oh, which measures the relative importance of viscous and surface tension effects, and the initial aspect ratio of the filament, $\mathcal{A}$. We investigate the influence of Oh over a wide range of aspect ratios. The small-Oh regime is characterized by the occurrence of a spherical blob at the extremity of the filament. This feature has a key impact on the tip dynamics, which moves with an oscillating velocity whose mean value is close to the Taylor-Culick prediction. The oscillatory behavior of the tip velocity is explained through a simple mass-spring model. This regime is also characterized by the presence of capillary waves, with a phase velocity slightly larger than the Taylor-Culick velocity. Surface oscillations are also observed when the filament reaches its final spherical shape; the corresponding period agrees well with predictions of the linear theory. At intermediate Oh and large $\mathcal{A}$, the tip velocity reaches a value close to the Taylor-Culick prediction. However, for smaller aspect ratios, the maximum tip velocity is much smaller than this prediction, and does not exhibit any oscillation. The recoil dynamics is qualitatively and quantitatively different at high Oh. In this case, the radius of the filament grows uniformly over time and no blob forms, making the tip velocity decrease after a short transient. A self-similar solution is found to closely match the numerical results in this regime.

I. INTRODUCTION

The capillary-driven retraction of liquid ligaments is involved in a broad variety of natural phenomena and industrial applications, such as break-up of ocean spume, atomization in fuel injectors or the ink-jet printing technology, to mention just a few [1]. Of particular interest in these applications is the prediction of the ligament's fate: will it break in a series of droplets or maintain its integrity and retract as a single drop. This information may be qualitatively obtained by equating the time needed for the capillary instability to develop to the time required for the filament to recoil [2]. Clearly, the tip velocity is a key quantity in such a model. However, despite much recent progress in the understanding of the retraction of viscous filaments, the detailed evolution of this velocity remains unclear. Improving the understanding of the mechanisms governing the tip velocity in various flow regimes is the primary goal of this paper.

Taylor [3] and Culick [4] independently showed that the tip velocity of a capillary-driven retracting inviscid planar sheet reaches a steady value, now referred to as the Taylor-Culick velocity. This formula was obtained by balancing surface tension and inertia effects, assuming that the mass of the retracting sheet accumulates in a circular rim.

---

* jean-lou.pierson@ifpen.fr

McEntee and Mysels [5] confirmed the Taylor-Culick prediction for soap films with a thickness larger than 1μm. In the limit where viscous effects are dominant, Brenner and Gueyffier [6] showed numerically that the retraction process changes dramatically: no rim forms, and the thickness of the entire sheet continuously increases over time. Despite this change of shape, the Taylor-Culick velocity is recovered in the long-time limit [7, 8]. However, recent experiments by Murano and Okumura [9] in a Hele-Shaw cell shed a new light on the range of validity of the Taylor-Culick model. In the viscously-dominated regime, the retraction velocity is governed by a capillary-viscous balance rather than a capillary-inertia balance. These results support in some sense the experimental findings of McEntee and Mysels [5] since the latter did not recover the Taylor-Culick prediction with very thin films (less than 1μm-thick) for which viscous effects dominate.

Pre-stretched axisymmetric filaments are prone to breaking up into a series of droplets provided viscous effects are small enough. Indeed, Notz and Basaran [10] and Schulkes [11] showed numerically the dramatic effect of the Ohnesorge number Oh on the retraction dynamics. For large Oh, *i.e.* effects of viscosity in the bulk and at the interface significantly larger than capillary effects, the filament may recoil and turn into a spherical drop without breaking up. In contrast, for small Oh, it frequently breaks into a series of droplets. A large stream of work has focused on the corresponding breakup mechanisms. Recently, Anthony et al. [12] performed an extensive numerical investigation of the retraction dynamics over a wide range of Ohnesorge number and initial aspect ratio $\mathcal{A}$, and proposed a classification of the different breakup modes as a function of these two control parameters. The end-pinching mechanism [13, 14] prevails at low Oh, while the classical Rayleigh-Plateau mechanism dominates at high Oh. For low Oh and intermediate $\mathcal{A}$, a different breakup mode, recently described by Wang et al. [15], may occur. This 'capillary wave breakup' mode, results from interactions of capillary waves travelling at the filament surface and originating from its ends. Still for low Oh, Hoepffner and Paré [16] observed that the filament may escape from end-pinching due to the formation and detachment of a Venturi-like flow inside the blob. This escape from pinching, which may occur at multiple times, results in a discontinuous variation of the critical aspect ratio leading to breakup as a function of Oh [12, 16].

The situation in which a filament recedes without breaking has received less attention. Keller [17] extended the initial analysis of Taylor and Culick for planar sheets to the case of axisymmetric filaments. His model was revisited by Hoepffner and Paré [16] and Pierson and Magnaudet [18] who pointed out that the original prediction for the corresponding 'Taylor-Culick' retraction velocity has to be lowered by a factor of $\sqrt{2}$. Notz and Basaran [10] showed that the blob velocity does not reach a steady value but rather oscillates about the Taylor-Culick velocity for Oh ≤ 0.1. Recently, Contò et al. [19] made use of a matched asymptotic expansion approach to determine the long-time filament profile. They identified three distinct regions, namely a steady section far from the tip, a growing spherical blob and an intermediate matching region. However, their analysis assumes the blob velocity to be given by the Taylor-Culick prediction, which significantly limits the generality of their conclusions. That the Taylor-Culick prediction provides a poor estimate of the actual tip velocity was recently emphasized in experiments performed by Planchette et al. [20] using inkjet printer heads. In these experiments, the tip velocities were consistently found to be significantly smaller than this prediction, and an empirical model accounting for viscous effects had to be designed to better fit the measured velocities.

The above review suggests that observations reported in the recent literature seriously question the actual range of validity of the Taylor-Culick prediction as a function of the Ohnesorge number and initial aspect ratio of the filament. The present paper is the first part of a detailed investigation aimed at shedding some light into this question. A companion paper [21] is devoted to the recoil velocity of a viscous planar sheet. In the present contribution, we focus on the recoil velocity of an axisymmetric filament, considering inertia-dominated and viscous-dominated regimes. To address the above question, we use a combination of physical arguments and fully-resolved simulations for three distinct values of the Ohnesorge number, namely Oh = 0.1 (inertia-dominated regime), Oh = 1 for which inertial and viscous effects have a similar magnitude, and Oh = 10 (viscously-dominated regime). The next section of the paper presents the problem under consideration, the foundations of the Taylor-Culick approximation, and the numerical methodology. The open source solver Basilisk is used to solve the axisymmetric governing equations of the two-phase medium with surface tension at the interface. The characteristics of this numerical approach are summarized in Sec. II D. Sections III and IV analyse the computational results obtained for Oh = 0.1 and Oh = $\{1, 10\}$, respectively. For low- and high-Oh values, the retraction velocity is compared with analytical models obtained using the long-wave approximation of the Navier-Stokes equations pioneered by Eggers and Dupont [22]. Our main findings are summarized in Sec. V.

II. PROBLEM AND METHODS
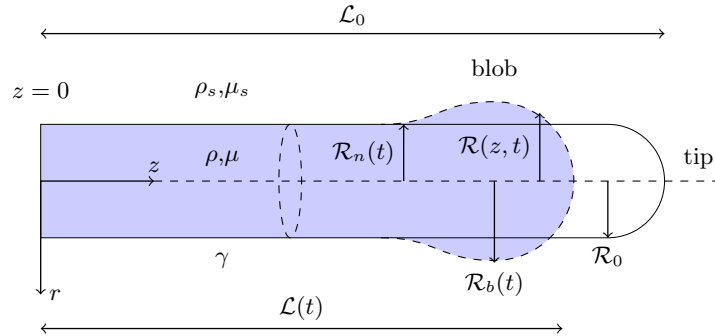
A. Problem description

FIG. 1: Sketch of the physical configuration, with the definition of the geometrical and physical parameters used throughout the paper.

We consider the retraction of a Newtonian viscous filament with initial length $2\mathcal{L}_0$ immersed in another Newtonian viscous fluid. Initially, the filament is assumed to be a long cylindrical column of radius $\mathcal{R}_0$ with semi-spherical ends, referred to as tips, and a mid-section located in the plane $z = 0$ (Fig. 1). We assume that both fluids are initially at rest. In real experiments, *e.g.* atomization of a jet, the filament has a more complex initial shape and the velocity within it is nonzero. Nevertheless this simple initial configuration, already widely used in previous investigations [10–12], provides a reference starting point to understand more realistic situations. Influence of the initial shape on the successive stages of the dynamics is discussed in Appendix A. The inner and outer fluids have densities ρ and ρ_s and dynamical viscosities μ and μ_s, respectively, and their common interface has an interfacial tension γ. The problem is characterized by four dimensionless parameters: the geometrical aspect ratio $\mathcal{A} = \mathcal{L}_0/\mathcal{R}_0$, the Ohnesorge number $\mathrm{Oh} = \mu/\sqrt{\rho\mathcal{R}_0\gamma}$, and the viscosity and density ratios ρ_s/ρ and μ_s/μ, respectively. To encompass both viscous-capillary and inertia-capillary regimes, the Ohnesorge number is selected in the range $0.1 \leq Oh \leq 10$. The lowest limit, $\mathrm{Oh} = 0.1$ is chosen to avoid complete pinching of the filament. The aspect ratio is varied in the range $5 \leq \mathcal{A} \leq 40$, which makes the long-wave approximation developed in [22] legitimate.

Although a surrounding fluid is always present in experiments [5, 9, 16, 20], its effects are not considered in most available numerical studies [10, 11]. An exception is Song and Tryggvason [23] who considered a retracting sheet in the small-Oh regime. For $\rho_s/\rho \leq 0.1$ and $\mu_s/\mu \leq 0.1$, they found the effect of the surrounding fluid to be minor. In the present work, the viscosity and density ratios are chosen such that the surrounding fluid has no influence on the retraction velocity. For this purpose, a density ratio $\rho_s/\rho = 0.01$ and a viscosity ratio $\mu_s/\mu = 0.001$ are selected. The same density ratio was used in [16] with a numerical approach similar to the one employed here.

B. Scaling analysis for a slender filament

Before performing a parametric numerical study, it is useful to define some characteristic quantities related to the retraction process. A suitable framework is the long-wave model derived by Eggers and Dupont [22]. Assuming that the drop is slender (*i.e.* its current radius $\mathcal{R}(z,t)$ and length $\mathcal{L}(t)$ are such that $\mathcal{R} \ll \mathcal{L}$), and neglecting effects of the surrounding fluid, the governing equations may be reduced to a pair of partial differential equations, namely

$$\frac{\partial \mathcal{R}^2}{\partial t} + \frac{\partial u_z \mathcal{R}^2}{\partial z} = 0 \tag{1}$$

$$\frac{\partial u_z}{\partial t} + u_z \frac{\partial u_z}{\partial z} = -\frac{\gamma}{\rho}\frac{\partial \kappa}{\partial z} + 3\frac{\mu}{\rho\mathcal{R}^2}\frac{\partial}{\partial z}\left(\mathcal{R}^2\frac{\partial u_z}{\partial z}\right). \tag{2}$$

In (1) and (2), u_z is the axial fluid velocity and κ denotes the local mean curvature whose definition reads

$$\kappa = \frac{1/\mathcal{R}}{\left(1 + (\partial\mathcal{R}/\partial z)^2\right)^{1/2}} - \frac{\partial^2\mathcal{R}/\partial z^2}{\left(1 + (\partial\mathcal{R}/\partial z)^2\right)^{3/2}}. \tag{3}$$

To leading order, κ tends toward $1/\mathcal{R}$ when $\mathcal{R}/\mathcal{L} \to 0$. Except for the mean curvature κ, the above set of equations is the lowest-order result of an asymptotic expansion of the axisymmetric Navier-Stokes equations with respect to the radial coordinate [22]. The longitudinal velocity u_z does not depend on the radial coordinate, while the radial velocity is assumed to be small but nonzero. To make this model valid in the tip vicinity, where the slope of the interface is very large, the full expression (3) of κ is employed in (2), instead of its lowest-order approximation $\kappa \approx 1/\mathcal{R}$. This combination is not the result of a formal asymptotic procedure, as the flow within the filament remains essentially one-dimensional. Nevertheless, the above model successfully describes the breakup of a liquid jet and the release of a drop from a circular orifice [22], as well as the retraction of a liquid ligament for Oh $= 1$ [10]. For Oh $= 0.01$, the latter authors pointed out that this model is unable to capture the pinching location. Indeed the occurrence of a vortex ring (which cannot be predicted in the framework of the long-wave approximation due to the limitation evidenced above) makes the ligament escape from pinch-off, as evidenced by [16]. In the present investigation, Oh is chosen large enough to prevent the occurrence of this phenomenon.

Equation (2) is normalized by defining dimensionless (starred) quantities as $u_z = U u_z^*$, $\kappa = \kappa^*/\mathcal{R}_0$, $z = \mathcal{L}_0 z^*$, $\mathcal{R} = \mathcal{R}_0 \mathcal{R}^*$ and $t = T t^* = (\mathcal{L}_0/U) t^*$. The characteristic scale U for the velocity is *a priori* unknown and must be determined *a posteriori*. The dimensionless form of (2) then becomes

$$\frac{\rho \mathcal{R}_0 U^2}{\gamma} \left(\frac{\partial u_z^*}{\partial t^*} + u_z^* \frac{\partial u_z^*}{\partial z^*} \right) = -\frac{\partial \kappa^*}{\partial z^*} + \frac{\mu U}{\gamma \mathcal{A}} \frac{3}{\mathcal{R}^{*2}} \frac{\partial}{\partial z^*} \left(\mathcal{R}^{*2} \frac{\partial u_z^*}{\partial z^*} \right). \tag{4}$$

In (4) the capillary term is chosen of order unity since it drives the whole motion in the regimes considered hereinafter. Two distinct asymptotic regimes take place when either inertia or viscous effects are negligible. If inertia effects balance the capillary force, (4) implies

$$U \equiv U_i = (\gamma/(\rho \mathcal{R}_0))^{1/2}, \tag{5}$$

which is the usual Taylor-Culick velocity [3, 4, 16, 18]; the associated time scale is $T = \mathcal{A} t_i$, with $t_i = (\rho \mathcal{R}_0^3/\gamma)^{1/2}$ the inertia-capillary time scale. In this regime, (4) may be re-written as

$$\frac{\partial u_z^*}{\partial t^*} + u_z^* \frac{\partial u_z^*}{\partial z^*} = -\frac{\partial \kappa^*}{\partial z^*} + \frac{Oh}{\mathcal{A}} \frac{3}{\mathcal{R}^{*2}} \frac{\partial}{\partial z^*} \left(\mathcal{R}^{*2} \frac{\partial u_z^*}{\partial z^*} \right). \tag{6}$$

In (6) the viscous term is negligible provided Oh $\ll \mathcal{A}$. Hence with Oh $= \mathcal{O}(1)$, inertia effects remain dominant if the initial aspect ratio of the filament is large enough. The second asymptotic limit corresponds to the situation in which viscous effects balance the capillary force. In this case, the characteristic velocity is $U = (\gamma/\mu)\mathcal{A} = U_v \mathcal{A}$, which is merely the product of the capillary velocity, $U_v = \gamma/\mu$, with the filament aspect ratio. The characteristic time scale is then the viscous-capillary time, *i.e.* $T \equiv t_v$ with $t_v = (\mu/\gamma)\mathcal{R}_0$. Inserting these scalings in (4) yields

$$\frac{\mathcal{A}^2}{Oh^2} \left(\frac{\partial u_z^*}{\partial t^*} + u_z^* \frac{\partial u_z^*}{\partial z^*} \right) = -\frac{\partial \kappa^*}{\partial z^*} + \frac{3}{\mathcal{R}^{*2}} \frac{\partial}{\partial z^*} \left(\mathcal{R}^{*2} \frac{\partial u_z^*}{\partial z^*} \right). \tag{7}$$

According to (7), inertia is negligible only if Oh $\gg \mathcal{A}$. Hence, even for large Oh, inertia remains significant if the initial aspect ratio is large enough.

C. Foundations of the Taylor-Culick approximation

For future purpose, it is useful to remind the governing set of equations and fundamental assumptions underlying the classical Taylor-Culick prediction. Details may be found in [8] for the two-dimensional case, and in appendix C of [18] for the axisymmetric geometry. In the latter reference it was showed that, provided assumptions to be detailed below are satisfied, integration of (1)-(3) from the symmetry plane ($z = 0$) to the tip ($z = \mathcal{L}$) yields the evolution of the total momentum of the filament $\mathcal{P} = \pi \rho \int_0^{\mathcal{L}} \mathcal{R}^2 u_z dz$ in the form

$$\frac{d\mathcal{P}}{dt} = \gamma \pi \mathcal{R}(z = 0) = \gamma \pi \mathcal{R}_0. \tag{8}$$

This result is obtained provided (*i*) $\mu \partial u_z/\partial z \approx 0$ at $z = 0$, so that viscous effects have no influence even though viscosity is nonzero; and (*ii*) the filament radius is uniform far from the tip, making the mean curvature reduce to $1/\mathcal{R}_0$ in the midplane $z = 0$. While the former assumption is not severe when the Ohnesorge number is small, it

becomes more questionable as Oh increases, since $z = 0$ is the origin of the extensional flow that takes place along the filament. Assumption (*ii*) is valid when the tip is far from the symmetry plane *i.e.* in the early stages of the retraction process, but it cannot hold during the late stages. Assuming in addition that (*iii*) the entire mass of fluid set in motion by the recoil process feeds a spherical blob in the tip region (see Fig. 1), while the cylindrical body of fluid in between the blob and the symmetry plane stays at rest, implies that $\mathcal{P}$ reduces to the blob momentum, $\mathcal{M}_b U_b$, where $\mathcal{M}_b$ stands for the mass of fluid enclosed within the blob and U_b is the velocity of the blob centre of mass. Assumption (*iii*) is questionable because a transition region necessarily stands in between the spherical blob with mean curvature $2/\mathcal{R}_b$ and the cylindrical body of the filament with mean curvature $1/\mathcal{R}$ [19, 24].

A final assumption is required to link U_b and $\mathcal{L}(t)$. Obviously, the simplest connection between the two is achieved by assuming that (*iv*) the velocity within the blob is uniform, in which case $U_b = -d\mathcal{L}/dt$. Actually, the velocity distribution cannot stay uniform, as the growth of the blob implies the existence a source-type flow within it. Nevertheless this assumption may be considered valid provided the blob radius grows at a rate much slower than $\mathcal{R}_0^{-1} d\mathcal{L}/dt$. Using (*iii*) and (*iv*), the mass flow rate entering the blob is $\dot{\mathcal{M}}_b \approx \pi \rho U_b \mathcal{R}_0^2$. Integrating over time and noting that the initial mass of the blob is $2\pi\rho\mathcal{R}_0^3/3$ implies that at any time $\mathcal{M}_b(t) = \pi\rho\mathcal{R}_0^2(\mathcal{L}_0 - \mathcal{L}(t)) + 2\pi\rho\mathcal{R}_0^3/3$. The blob momentum being initially zero, integration of (8) yields

$$\frac{d\mathcal{L}}{dt}\left(\mathcal{L}_0 - \mathcal{L} + \frac{2}{3}\mathcal{R}_0\right) + \frac{\gamma t}{\rho\mathcal{R}_0} = 0 \,. \tag{9}$$

Making use of the initial condition $\mathcal{L}(t = 0) = \mathcal{L}_0$, integration of (9) provides the blob velocity as

$$U_b = \frac{U_i t}{\left(t^2 + \frac{4}{9}t_i^2\right)^{1/2}} \,. \tag{10}$$

D. Governing equations and numerical method

The variable-density and viscosity Navier-Stokes equations with surface tension are written in the form

$$\boldsymbol{\nabla} \cdot \mathbf{u} = \mathbf{0} \quad, \tag{11}$$

$$\rho\left(\frac{\partial\mathbf{u}}{\partial t} + \mathbf{u} \cdot \boldsymbol{\nabla}\mathbf{u}\right) = -\boldsymbol{\nabla}p + \boldsymbol{\nabla} \cdot (2\mu\mathbf{D}) + \mathbf{f}_\gamma \quad, \tag{12}$$

$$\frac{\partial\rho}{\partial t} + \boldsymbol{\nabla} \cdot (\rho\mathbf{u}) = 0 \quad, \tag{13}$$

where $\mathbf{u}$ denotes the fluid velocity, p the pressure, $\mathbf{D}$ the strain-rate tensor, and $\mathbf{f}_\gamma$ is the local density of the capillary force per unit volume. Equations (11)-(13) are solved thanks to the approach implemented in the Basilisk open source code [25]; see http://basilisk.fr. The corresponding finite-volume spatial discretization makes use of a graded quadtree partitioning. All variables are collocated at the cell center. A piecewise-linear geometrical Volume of Fluid method is used to solve (13) [26]. Time advancement of the viscous term in the momentum equation is achieved with an implicit scheme, while the advection equation is solved using the Bell-Colella-Glaz algorithm [27]. Incompressibility is enforced at the end of the time step through a projection technique. The heat equation and the Poisson equation respectively resulting from the implicit treatment of viscous terms and from the projection technique are solved thanks to a multigrid solver, the relative tolerance of which is chosen to be less than 1×10^{-5} in all cases. A consistent discretization of the pressure and the capillary force is also used to avoid parasitic currents (see Popinet [28] for more details).

Axisymmetric computations are performed on a fixed grid in a cylindrical domain with a square cross section. The outer boundaries are located sufficiently far away from the filament to avoid confinement effects. For this purpose the length of the domain is set to $\mathcal{L}_0 + 5\mathcal{R}_0$ (Fig. 2). Rotational symmetry is imposed on the filament axis ($r = 0$), while standard symmetry conditions are imposed on all other boundaries. The grid is more refined in the central region corresponding to the filament and its immediate surroundings, $0 \leq r \leq 3\mathcal{R}_0 - 4\mathcal{R}_0$ (depending on the initial aspect ratio), so as to properly describe the flow within the filament and the boundary layers on both sides of the interface. Depending on Oh, at least 20 cells (for large Oh) and up to approximatively 80 cells (for low Oh) per initial filament radius are uniformly distributed in this region. In comparison, 16 radial elements stand along the filament radius in the simulations of Anthony et al. [12]. In the outer region, $r \geq 3\mathcal{R}_0 - 4\mathcal{R}_0$, the grid is uniform in the axial (z) direction but the cell size increases with r. More specifically, this size doubles every time r increases by $0.5R_0$, until a maximum cell size of approximatively $\mathcal{R}_0/2$ is reached. A specific refinement aimed at capturing the filament
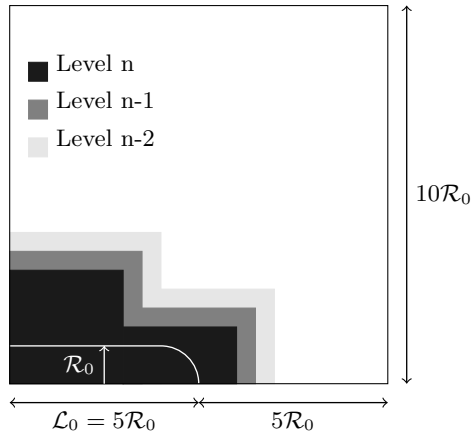
FIG. 2: Sketch of the computational domain for $\mathcal{A} = 5$. Each grey region corresponds to a specific level of grid refinement. The cell size varies by a factor of 2 in between two successive levels.

dynamics in the late stages (*i.e.* when the tip gets close to the symmetry plane $z = 0$) is achieved in the region $0 \leq z \leq 3\mathcal{R}_0 - 4\mathcal{R}_0$ for $r \leq 6\mathcal{R}_0$. Figure 2 illustrates these choices in the case $\mathcal{A} = 5$. A specific script used to run the simulations presented in this paper may be found in [29].

III.   LOW OHNESORGE NUMBER: $\mathbf{Oh} = 0.1$

In what follows we examine the tip velocity of a retracting filament, from the very beginning of the recoil until the stage where the filament has virtually recovered its equilibrium spherical shape. In this section we focus on the low-but-finite value $\mathrm{Oh} = 0.1$, with four initial aspect ratios, $\mathcal{A} = \{5, 10, 20, 40\}$. In the next section, we shall consider two higher values of the Ohnesorge number, namely $\mathrm{Oh} = \{1, 10\}$. It must be stressed that under such conditions, the filament is not expected to break up according to the regime map provided by [12].

We start by considering the low-but-finite Oh conditions under which viscous effects are expected to play only a secondary role in the blob region during the retraction process. The 'secondary role' terminology must not be misunderstood. Indeed, the simulations in [10] and [12] reveal dramatic differences in the ultimate fate of filaments with a given $\mathcal{A}$ in the range $0 < Oh \leq 0.1$. Nevertheless, as none of the ligaments considered here is expected to break up, this terminology is relevant for the problem on which the present paper focuses.
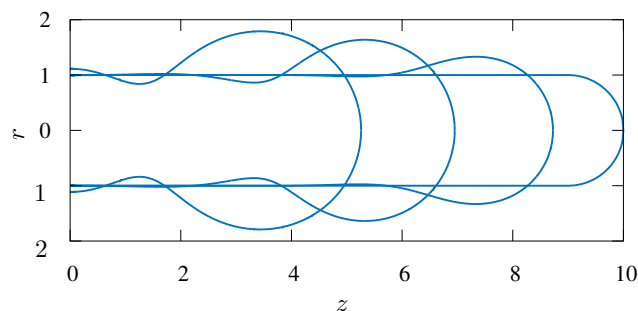
A.   Early stage

FIG. 3: Successive shapes of a retracting filament with $\mathrm{Oh} = 0.1$ and $\mathcal{A} = 10$ (assuming $\mathcal{R}_0 = 1$). The time step between two successive snapshots is $\Delta t = 2t_i$.

Figure 3 displays the early evolution of the interface. As the filament recedes, most of its surface retains its initial

cylindrical shape while a spherical blob forms at the tip, as observed in previous low-Oh investigations, especially the pioneering simulations by Notz and Basaran [10]. Thus present low-Oh results support assumptions (ii) and (iii) discussed in Sec. II C. Figure 4 displays the numerical evolution of the tip velocity, defined as $U_t = -\mathrm{d}\mathcal{L}/dt$, for four

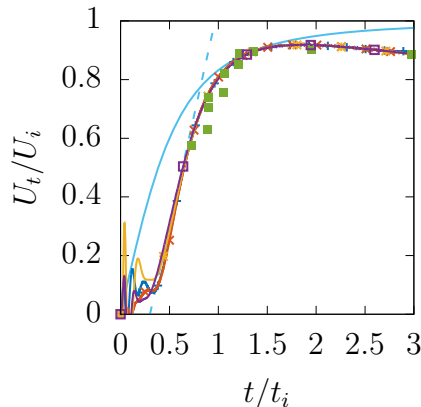
FIG. 4: Tip velocity versus time during the early stages of the retraction process for Oh $= 0.1$ and different initial aspect ratios. $-+-$: $\mathcal{A} = 5$, $- \times -$: $\mathcal{A} = 10$, $- * -$: $\mathcal{A} = 20$, $-\square-$: $\mathcal{A} = 40$, $-$: prediction (10), $--$: guide for the eye with slope $3U_i/(2t_i)$, ■: numerical results from [10] for $\mathcal{A} = 15$.

different initial aspect ratios. Numerically, this velocity is obtained by determining the tip position ($z = \mathcal{L}$) using the height function defined in [26], combined with a simple upwind scheme. Except at the very beginning of the recoil, say $0 \leq t/t_i \leq 0.4$, U_t is found to be independent from the initial aspect ratio, since all curves collapse onto a master curve. Hence, for small Oh, $\mathcal{A}$ does not influence the evolution of $U_t \approx U_b$, as (10) predicts. Significant oscillations of the tip velocity are observed at the very beginning of the recoil process, making the initial evolution of U_t depart from (10). These oscillations have two distinct origins. First, given the selected initial shape of the ligament, an abrupt $1/\mathcal{R}_0$-jump in the mean curvature takes place in the plane where the cylindrical column connects to the hemispherical end. Then, for numerical reasons similar to those discussed in [26] in the case of a static drop, there is a transient imbalance between the computed capillary force evaluated from the prescribed initial shape and the computed pressure gradient. The disturbances resulting from these two sources generate capillary waves which are gradually damped by viscous effects within the ligament. The oscillations observed in Fig. 4 are not specific to the initial geometry selected here. In Appendix A, we show that selecting a different initial shape (corresponding to a prolate spheroidal tip region) also yields the generation of such oscillations. The two evolutions of the tip velocity are found to be markedly different for $t \lesssim t_i$, but become very close to each other beyond this initial transient. Another indication that this transient does not affect significantly the upcoming behavior is provided by the comparison with results from Notz and Basaran [10] obtained with a finite-element discretization. As Fig. 4 shows, the evolution of the tip velocity extracted from the figure 22 of the latter reference (with $\mathcal{A} = 15$) is very close to that observed in the present simulations for $t \gtrsim t_i$.

Another entirely physical mechanism makes (10) unable to predict the early evolution of U_t. Considering that the blob radius grows uniformly with radial velocity $\dot{\mathcal{R}}_b$, the tip recedes with velocity $U_b - \dot{\mathcal{R}}_b$, while the front of the blob recedes with velocity $U_b + \dot{\mathcal{R}}_b$, resulting in an entering flow rate $\pi \mathcal{R}_0^2(U_b + \dot{\mathcal{R}}_b)$. At very short times, the blob is still almost a half-sphere, the volume of which changes at a rate $2\pi \mathcal{R}_0^2 \dot{\mathcal{R}}_b$, implying $\dot{\mathcal{R}}_b = U_b$. Hence, radial velocities at the blob surface are initially of the order of U_b, making the velocity distribution within the blob significantly not uniform and therefore contradicting assumption (iv) in Sec. II C. Nevertheless, (10) is seen to reduce to $U_b/U_i \sim 3t/(2t_i)$ in the short-time limit $t/t_i \ll 1$, and the corresponding prediction for the acceleration, $\dot{U}_b = \gamma/(\rho \mathcal{R}_0^2)$, closely agrees with the numerical evolution shown in Fig. 4 beyond the initial oscillation period. It is quite surprising that the pre-factor in the right-hand side of (8) and the assumption of an initially spherical blob geometry provide a good estimate of the initial tip acceleration, despite the fact that all conditions required for (8) to hold are not satisfied. This makes us suspect that this agreement is partly fortuitous. Indeed, in Appendix A we show that the initial tip acceleration highly depends on the initial geometry of the tip region. More computations are thus required to properly delineate the effect of the initial geometry of the end region on the initial tip acceleration.

B. Intermediate stage

Beyond the acceleration stage, Fig. 4 reveals a striking characteristics: whatever the filament aspect ratio in the considered range, the long-term tip velocity does not reach the Taylor-Culick prediction U_i. Rather this velocity starts to decrease for $t \gtrsim 2t_i$. To further investigate the mechanisms that govern this evolution, it is desirable to introduce a time scale that properly normalizes the duration of the recoil process irrespective of the aspect ratio. Since U_t has been found to be independent from $\mathcal{A}$, the relevant time scale is $\mathcal{A}t_i$; this is also the time scale ensuring the balance between capillary and inertial effects in (6).
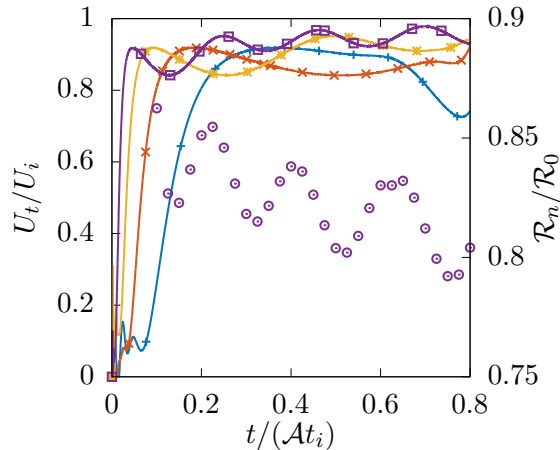

FIG. 5: Tip velocity and neck radius *vs.* time for Oh $= 0.1$ and different aspect ratios $-+-$: $\mathcal{A} = 5$, $-\times-$: $\mathcal{A} = 10$, $-*-$: $\mathcal{A} = 20$, $-\square-$: $\mathcal{A} = 40$. $\odot$: neck radius for $\mathcal{A} = 40$.

Figure 5 displays the tip velocity from the beginning of the retraction until the moment at which the tip approaches the midplane $z = 0$. The evolution of the neck radius $\mathcal{R}_n$, defined as the minimum radius located just in front of the blob (see Fig. 1), is also displayed. This representation makes new features apparent. For $\mathcal{A} = 5$, the tip velocity reaches a maximum close to $0.9U_i$ and starts decreasing for $t/\mathcal{A}t_i \approx 0.3$. In contrast, for $\mathcal{A} > 10$, U_t oscillates about an average value which, over the time interval displayed in the figure, is close to 0.9 but slowly increases over time (this is especially clear for $\mathcal{A} = 40$). These observations are in line with those of Notz and Basaran [10] who, for the same Oh and $\mathcal{A} = 15$, found the tip velocity to exhibit damped oscillations about an average value $U_t \approx 0.83$. While the magnitude of the oscillations seen in Fig. 5 does not significantly depend on $\mathcal{A}$, the number of periods increases with $\mathcal{A}$. The frequency of the oscillations is also found to be independent from the aspect ratio when $\mathcal{A}$ is large enough. Indeed, once expressed with respect to t_i instead of $\mathcal{A}t_i$, the time period is found to be ≈ 9 and 8.8 for $\mathcal{A} = 40$ and $\mathcal{A} = 20$, respectively. Figure 5 also shows (for $\mathcal{A} = 40$) that this oscillatory behavior is associated with small oscillations in the neck radius, with some phase shift between the tip velocity and neck radius oscillations. The amplitude of the latter is approximately $0.02\mathcal{R}_0$. Injecting this value in (5) as if the radius of the filament were oscillating at every longitudinal position in the same way as the neck, yields oscillations of the tip velocity of the order of $0.01U_i$, which is typically $2-3$ times smaller than the amplitude observed in Fig. 5. Moreover, the figure reveals that the two quantities approximately oscillate in quadrature, while (5) predicts that they should oscillate phase-opposed. Hence, while there is little doubt that variations of the tip velocity and oscillations of the neck radius are closely connected, the coupling between them cannot be understood directly through (5). In other words, the framework of the Taylor-Culick approximation is too simple to account for this coupling.

The mechanism responsible for the tip oscillations may be understood and quantified through the following simple mass-spring model. From $t_0 = t_i/3$ until $t = t_i$, we assume that the velocity of the blob center of mass is $U_b(t) \approx \frac{3}{2}U_i\frac{t-t_0}{t_i}$, which corresponds to the dotted line in Fig. 4. Then $U_b(t)$ stays close to U_i for $t_i \leq t \leq 2t_i$, beyond which the oscillations set in, starting with a decrease of $U_b(t)$ (see Figs. 4 and 5). The mass increase of the blob from $t = t_0$ up to $t = 2t_i$ is $\pi\rho\mathcal{R}_0^2 \int_{t_0}^{2t_i} U_b(t)dt = \frac{4\pi}{3}\rho\mathcal{R}_0^3$. Since the initial mass of the hemispherical blob is $\frac{2\pi}{3}\rho\mathcal{R}_0^3$, its total mass at time $t = 2t_i$ has increased to $2\pi\rho\mathcal{R}_0^3$. Assuming that the blob has reached an almost spherical shape at $t = 2t_i$ and keeps it at later times, any further variation of the blob radius by an amount x changes the restoring capillary force in the plane of the forming neck by $2\pi\gamma x$. In the reference frame of the neck, it also changes the tip
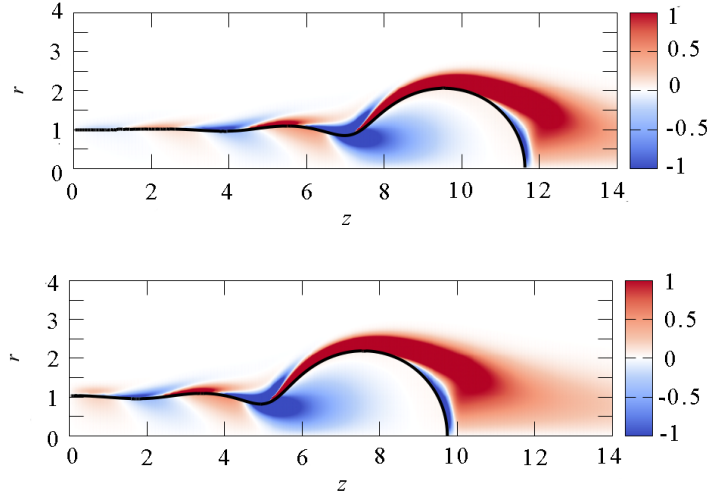
FIG. 6: Interface and vorticity contours for Oh $= 0.1$ and $\mathcal{A} = 20$ at: (a) time $t/t_i = 10$, and (b) time $t/t_i = 12$; the azimuthal vorticity ω_θ is normalized with $U_i/\mathcal{R}_0$.

velocity by $-2dx/dt$, since the distance from the tip to the neck increases by $2x$. Therefore, if the blob is schematically considered as a point mass $2\pi\rho\mathcal{R}_0^3$ standing at the tip, any variation in the rate of change of the blob radius, *i.e.* in dx/dt, results in an inertia force $-4\pi\rho\mathcal{R}_0^3 d^2 x/dt^2$ at the tip. This situation is equivalent to a mass-spring system with mass $m = 4\pi\rho\mathcal{R}_0^3$ and stiffness $k = 2\pi\gamma$, the radian frequency of which is $\Omega = (k/m)^{1/2} = \left(\frac{\gamma}{2\rho\mathcal{R}_0^3}\right)^{1/2} = 1/(\sqrt{2}t_i)$. Hence, for $t \gtrsim 2t_i$, further variations of the blob radius induce oscillations of the tip velocity with a characteristic period $T_\Omega = 2\pi/\Omega = 2\pi\sqrt{2}t_i \approx 8.89t_i$. According to this model, one should have $T_\Omega/\mathcal{A}t_i = 8.89\mathcal{A}^{-1}$, a prediction which agrees within 2% with the periods determined from Fig. 5 for $\mathcal{A} = 20$ and 40. Although this excellent agreement is certainly partly fortuitous, given the rough assumptions of the model, this prediction gives a strong support to the mechanism on which this model is grounded. That is, assuming that the variations of the blob radius dictate those of both the tip velocity and the capillary force at the neck for $t \gtrsim 2t_i$ is sufficient to predict quantitatively the frequency of the oscillations observed in the former. It is worth noting that the radius of a spherical drop with a volume $2\pi\mathcal{R}_0^3$ corresponding to that of the blob at time $t = 2t_i$ is $(3/2)^{1/3}\mathcal{R}_0$ so that, according to the dispersion relation (15) below, its fundamental oscillation frequency is $2\sqrt{2/3} \approx 1.63$ times larger than Ω. Hence, the tip is found to oscillate with a frequency approximately 40% lower than that of the capillary oscillations of the drop 'equivalent' to the blob. Additional computations with a different initial tip geometry, such as those reported in Appendix A, indicate that the influence of this initial condition extends over a transient that ends in the range $1 \lesssim t/t_i < 2$. This suggests that the above conclusions, expected to apply only for $t > 2t_i$, hold irrespective of the details of the initial shape of the filament.

The tip oscillations play the role of a wavemaker and trigger the formation of capillary waves upstream of the growing blob. The propagation of these waves along the cylindrical part of the filament is illustrated in Fig. 6. Positive and negative vortical regions alternate on both sides of the interface, as already noticed by Gordillo et al. [24] (for 2D sheets) and Wang et al. [15]. The origin of this vorticity pattern is readily understood by noting that the vorticity at the free surface is directly proportional to the product of the axial curvature and tangential velocity [30]. The former changes sign every half wavelength while the latter does not, yielding the observed alternate pattern. It is to be noticed that in the above scenario, alternation of positive and negative vorticity is seen as a consequence of the existence of capillary waves, themselves resulting from tip oscillations. This differs from (but does not contradict) the mechanism suggested in [23] and [15], according to which the interaction between the positive vorticity at the blob surface and the negative one in the neck region yields a tertiary vortex carrying positive vorticity upstream of the neck, which imposes a local increase in the radius of the filament. This process being self-repeating, [23] and [15] proposed that the alternation of positive and negative vorticity produces the capillary wave train. Thus, what is seen as a consequence of the oscillations of the tip velocity in the mechanism proposed here is considered as the origin of the capillary waves in the aforementioned two studies which ignored these oscillations.

Simulations with $\mathcal{A} = 20$ and $\mathcal{A} = 40$ yield the same wavelength for the capillary waves, $\lambda \approx 3.25\mathcal{R}_0$. With Oh $= 0.01$ and $\mathcal{A} = 25$, Wang et al. [15] also observed capillary waves that keep an almost constant wavelength,

$\lambda \approx 3\mathcal{R}_0$. Gathering the two sets of results suggests that the wavelength is independent from the filament aspect ratio when $\mathcal{A}$ is large enough, and only weakly depends on Oh for Oh ≤ 0.1. It must be observed that in both cases λ is less than $2\pi\mathcal{R}_0$, the shortest wavelength that may become unstable due to the Rayleigh-Plateau instability. The corresponding inviscid dispersion relation for small stable disturbances [31] may be written in the form

$$\left(\frac{c}{U_i}\right)^2 = \frac{(k\mathcal{R}_0)^2 - 1}{k\mathcal{R}_0} \frac{I_0'(k\mathcal{R}_0)}{I_0(k\mathcal{R}_0)}, \tag{14}$$

where $c(k)$ is the phase velocity of the disturbance with wavenumber $k = 2\pi/\lambda$ and I_0 denotes the zeroth-order Kelvin function. Inserting the observed value of λ in (14) yields $c \approx 1.18U_i$, which suggests that the capillary waves are travelling slightly faster than the tip. This prediction is confirmed quantitatively by comparing the distance travelled by a crest or a trough of the wavetrain in between the top and bottom panels of Fig. 6 with the distance travelled by the tip during the same time lapse. It turns out that the former is approximately 1.17 times larger than the latter. The oscillation period of the capillary waves may be estimated as $\lambda/c \approx 2.75t_i$, a value approximatively 3 times smaller that the oscillation period of the tip ($8.89t_i$). This reinforces our statement that the tip oscillation triggers the formation of capillary waves and not the other way around.
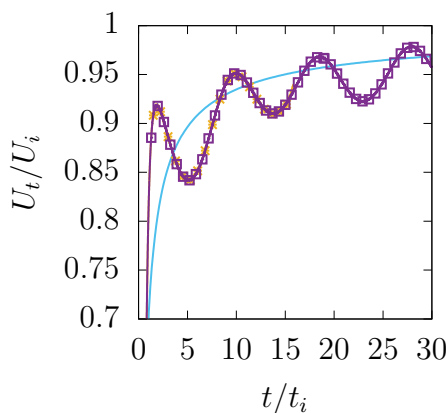

FIG. 7: Tip velocity *vs.* time for Oh $= 0.1$ and different initial aspect ratios. $-*-$: $\mathcal{A} = 20$, $-\square-$: $\mathcal{A} = 40$, $-$: $U_i\left(1 - (6t_i/t)^{2/3}\right)$.

To close the loop, let us finally come back to the origin of the deviation between the evolution of the tip velocity and the Taylor-Culick prediction for $t > t_i$. In the long-term limit $t \gg t_i$, the blob radius $\mathcal{R}_b(t)$ is much larger than $\mathcal{R}_0$. The blob volume now results essentially from the cumulated flow through the neck since the beginning of the recoil, so that $\frac{4}{3}\pi\mathcal{R}_b^3 \approx \pi\mathcal{R}_0^2 U_b t$, assuming that the blob velocity stayed approximately constant in the meantime. The rate of change of the blob radius then obeys approximately $4\pi\mathcal{R}_b^2\dot{\mathcal{R}}_b \approx \pi\mathcal{R}_0^2 U_b$ which, assuming $U_b \approx U_i$, implies $\dot{\mathcal{R}}_b \approx (6t_i/t)^{2/3}U_i$. Therefore the tip velocity is expected to approach the Taylor-Culick value following the law $U_t(t) = U_i - \dot{\mathcal{R}}_b(t) \approx U_i\left(1 - (6t_i/t)^{2/3}\right)$. As Fig. 7 shows, this prediction is in fairly good agreement with the numerical evolutions observed with long filaments. This agreement makes the origin of the deviation $U_i - U_t(t)$ clear: as far as the growth of the blob induces a significant radial velocity $\dot{\mathcal{R}}_b$, the fluid velocity within the blob cannot be uniform, contradicting assumption (iv) in the Taylor-Culick argument (see Sec. II C). Sünderhauf et al. [7] reported similar observations for a retracting planar sheet in the low-Oh regime. In this case, the tip velocity first reaches a plateau corresponding to $U_t \approx 0.8U_i$, before tending gradually toward U_i. So, in all cases, the Taylor-Culick velocity is reached only after the recoil has lasted long enough for the assumption of a uniform velocity within the blob to become realistic. Obviously this requires the initial aspect ratio $\mathcal{A}$ to be large enough for the condition $t \gg t_i$ to be met without the filament breaking up in the meantime or already collecting into an approximately spherical drop. At this point, it is probably relevant to quote Keller who concluded his extension of the Taylor-Culick model to cylindrical threads in [17] as follows (using present notations): *The present analysis [...] cannot be viewed as a precise theory, but rather as an indication of the way in which the various parameters influence the motion of the edge [...]. However its results are probably asymptotic to the exact hydrodynamic results for gradually varying threads and films for times long compared to some characteristic time. For an initially uniform thread of radius $\mathcal{R}_0$ [...], the characteristic time is $t_i = (\rho\mathcal{R}_0^3/\gamma)^{1/2}$.*
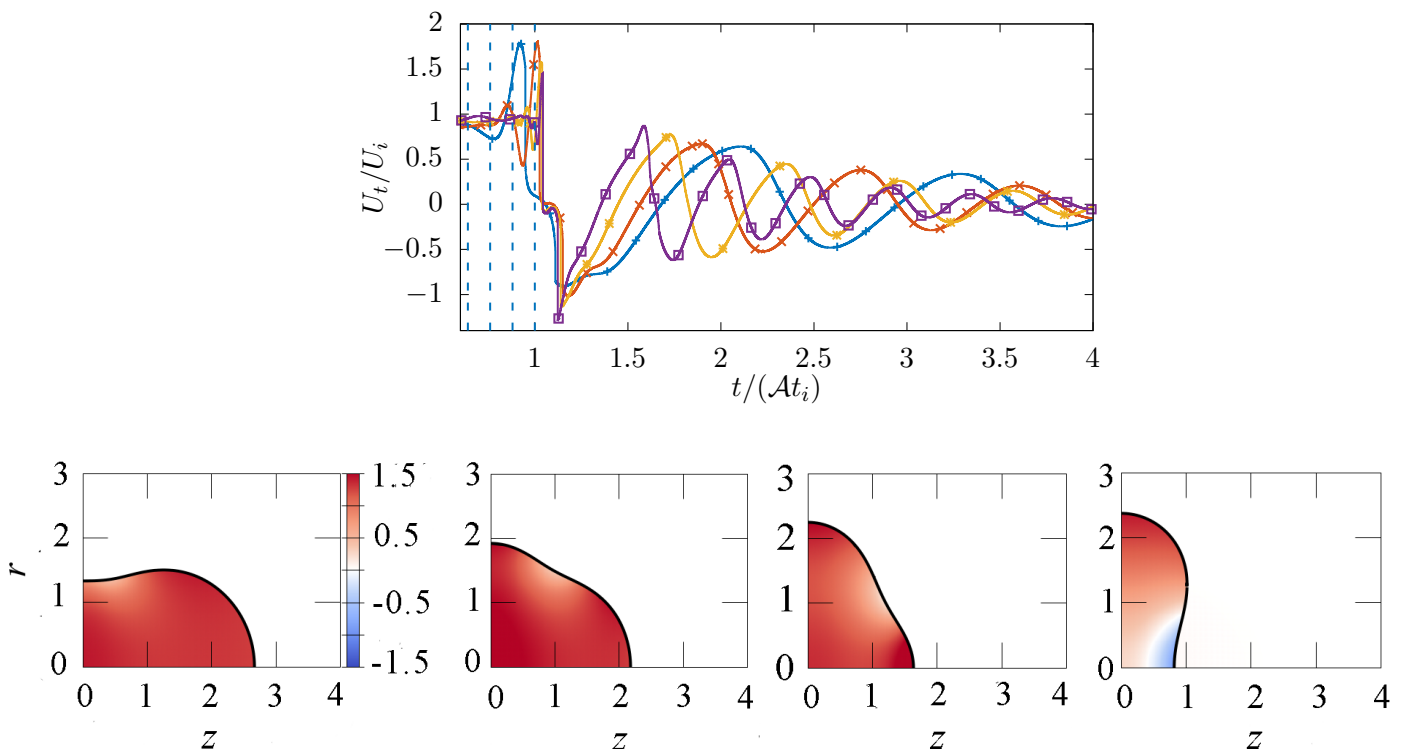
C. Final stage

FIG. 8: Late evolution of the filament for Oh = 0.1 and different aspect ratios. Top row: tip velocity. $-+-$: $\mathcal{A} = 5$, $-\times-$: $\mathcal{A} = 10$, $-*-$: $\mathcal{A} = 20$, $-\square-$: $\mathcal{A} = 40$. Bottom row: distribution of the normalized pressure $p/(\rho U_i^2)$ within the filament for $\mathcal{A} = 5$. Snapshots in the bottom row are taken at time instants (increasing from left to right) identified with a vertical dotted line in the top figure; the time step between two successive images is $0.6 t_i$.

Provided the filament does not break up at some point of the recoil, the final stage of its evolution starts when the dimensionless time $t/(\mathcal{A}t_i)$ becomes of order unity. Then the filament aspect ratio becomes of $\mathcal{O}(1)$ and the surface oscillates before the spherical equilibrium shape is recovered. Figure 8 (top) displays the evolution of the dimensionless tip velocity U_t/U_i for four different initial aspect ratios. Whatever $\mathcal{A}$, the tip velocity surpasses the Taylor-Culick prediction at some instant of time such that $t = \mathcal{O}(t_i\mathcal{A})$, reaching values $U_t/U_i \approx 1.8$ before abruptly falling down to $U_t/U_i \approx -1$. These positive and negative peaks in the tip velocity may be interpreted in terms of capillary pressure. This is made clear by comparing the evolution of U_t (top row in Fig. 8) and that of the pressure distribution within the filament (bottom row). In the left frame, the latter is made of a quasi-spherical blob connected to what remains of the cylindrical column, the length of which is of $\mathcal{O}(\mathcal{R}_0)$. The capillary pressure inside the blob is approximately constant. In the next two frames, the cylindrical column is gone and a wave starting from the top of the blob and moving toward its axis makes the curvature within the (z, r) plane become locally negative. The increased curvature in the tip region results in a pressure maximum there, yielding a strong increase in the tip velocity. The wave then propagates in the opposite direction (last frame in the bottom row), making the pressure reach a minimum on the axis, which yields a strong decrease in the tip velocity. This process repeats itself but viscous damping makes the oscillation amplitude decrease and the filament eventually relaxes toward its equilibrium spherical shape. The period and decay rate of the observed oscillations may be compared to the classical predictions of the linear Rayleigh-Lamb theory, namely [32]

$$\omega_l = \sqrt{\frac{\gamma}{\rho\mathcal{R}_f^3}(l-1)l(l+2)}, \quad \beta_l = \frac{\mu(l-1)(2l+1)}{\rho\mathcal{R}_f^2} \tag{15}$$

where l is the considered mode of oscillation in the usual nomenclature of spherical harmonics, ω_l and β_l are the radian frequency and decay rate of mode l, respectively, and $\mathcal{R}_f$ is the final equilibrium radius of the filament $(\mathcal{R}_f/\mathcal{R}_0 \approx (3\mathcal{A}/2)^{1/3}$, assuming $\mathcal{A} \gg 1)$. For obvious symmetry reasons, only even modes can exist in the present

configuration. Moreover, in the early stage of the recoil, the curvature changes sign in the transition region between the cylindrical body of the filament and the blob. Since the surface would keep a positive curvature everywhere if only the mode $l = 2$ were present, mode $l = 4$ is necessarily involved. Indeed, expanding the interface position in the (r, z)-plane into spherical harmonics reveals that these two modes dominate the deformation of the interface. More specifically, mode $l = 4$ is initially dominant but is gradually superseded by mode $l = 2$. For the latter, predictions (15) yield

$$\frac{T_o}{t_i} = \pi\sqrt{\frac{3\mathcal{A}}{4}}\,, \quad \beta t_i = 5\left(\frac{3}{2}\mathcal{A}\right)^{-2/3} Oh\,. \tag{16}$$
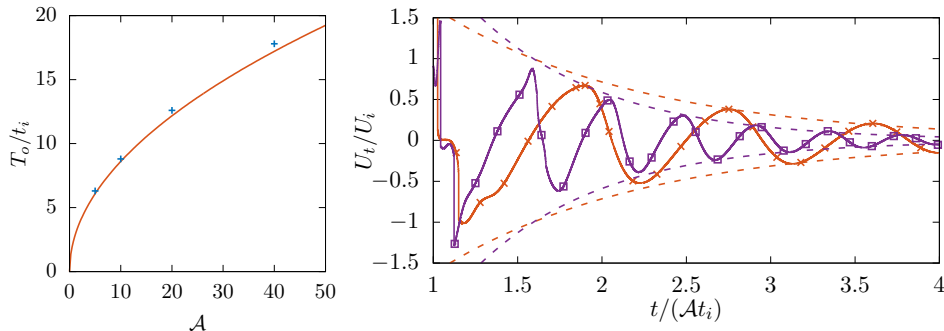

FIG. 9: Characteristics of capillary oscillations during the final stage for $Oh = 0.1$. Left: period of the oscillations *vs.* the initial aspect ratio, $\mathcal{A}$; +: Simulation results, −: linear prediction (16) for mode $l = 2$. Right: final decay of the oscillations *vs.* time; $-\times-$: $\mathcal{A} = 10$, $-\square-$: $\mathcal{A} = 40$, dotted line: linear prediction (16) for mode $l = 2$.

Figure 9 compares the numerical results obtained for $t \gtrsim \mathcal{A}t_i$ with the above predictions. The observed period agrees well with the first of (16), even though the oscillation amplitudes are large. The agreement on the decay rate is quite poor for $t \leq 2\mathcal{A}t_i$, presumably because the nonlinearities dissipate a substantial part of the kinetic energy of the oscillations. At later times, the oscillation amplitudes are much reduced and the observed decay rate is in better agreement with the predictions provided by the second of (16). The same prediction also gives insight into the subtle dependence of the decay rate with respect to $\mathcal{A}$, as observed in Fig. 8. Selecting t_i as the time scale, the decay rate is found to be a decreasing function of $\mathcal{A}$. In contrast, normalizing β with $\mathcal{A}t_i$ makes the dimensionless decay rate proportional to $\mathcal{A}^{1/3}$. This weak increase of $\mathcal{A}t_i\beta$ with the filament aspect ratio is the reason why in Fig. 8 the oscillations have a slightly smaller amplitude for $\mathcal{A} = 40$ than for $\mathcal{A} = 5$ at a given dimensionless time.

IV.   MODERATE AND HIGH OHNESORGE NUMBERS

A. $Oh = 1$

Figure 10 displays the evolution of the tip velocity at $Oh = 1$ for four initial aspect ratios. According to the left panel, the initial acceleration process is only weakly dependent on the aspect ratio, and becomes virtually independent from it for $t/t_i \gtrsim 0.7$. It is strikingly different from the evolution predicted by (10). Indeed, with $Oh = 0.1$, Fig. 4 indicates that the maximum tip velocity is reached at $t/t_i \approx 1.5$, while in the present case, it takes twice as long to reach this maximum in the case of the shortest filament, and even longer for the more slender ones. Beyond a short initial transient, say for $t/t_i \gtrsim 0.5$ with $\mathcal{A} = 40$, the computed evolutions for long enough filaments ($\mathcal{A} \geq 10$) are in excellent agreement with those reported in [10] for $\mathcal{A} = 15$. The right panel displays the complete evolution of the tip velocity *vs.* the dimensionless time $\mathcal{A}t_i$ throughout the 'life' of the filament. For sufficiently high $\mathcal{A}$, the tip velocity almost reaches a plateau where it is close to the Taylor-Culick prediction. In contrast, no such plateau takes place for $\mathcal{A} \leq 10$. No oscillations are observed during the final stage with such short filaments. Instead, the tip velocity monotonically tends to zero. Only for $\mathcal{A} \geq 20$ is a reversal of the tip velocity observed, before the filament comes to rest. This might seem paradoxical at first glance, since the second of (16) predicts a slight increase of the decay rate with the aspect ratio, once normalized with $\mathcal{A}t_i$. However, the shape oscillations result from a conversion of kinetic energy into surface energy and *vice versa*, and the figure indicates that the larger $\mathcal{A}$ the larger the maximum of the tip velocity is. Therefore, the longer the filament the larger the available kinetic energy at the beginning of the final
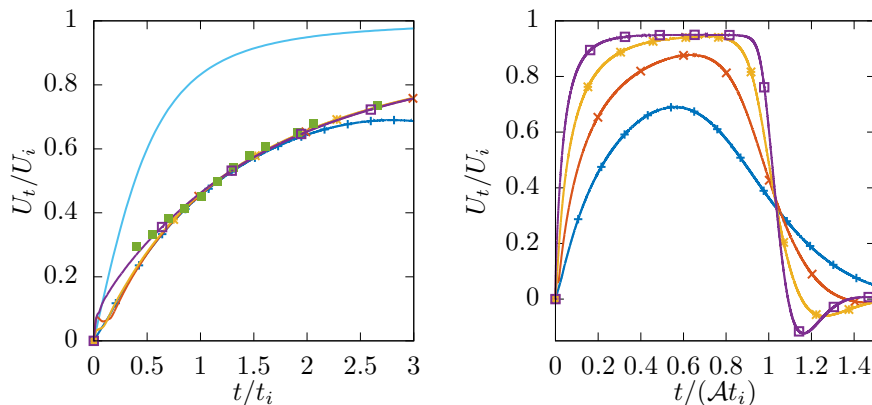
FIG. 10: Tip velocity *vs.* time for a filament with Oh = 1 and different initial aspect ratios. Left: early stage of recoil; right: intermediate and late stages. $-+-$: $\mathcal{A} = 5$, $-\times-$: $\mathcal{A} = 10$, $-*-$: $\mathcal{A} = 20$, $-\square-$: $\mathcal{A} = 40$; $-$: short-time prediction (10), ■: numerical results from [10] for $\mathcal{A} = 15$.

stage is. This influence of the aspect ratio on the kinetic energy turns out to surpass that on the decay rate, making long filaments more prone to oscillate during the final stage.

B.   Early stage of recoil for Oh $\gg$ 1

When the Ohnesorge number is large, the recoil is mostly slowed down by viscous effects rather than inertia. Therefore the tip velocity is primarily dictated by a balance between contributions of viscosity and surface tension, as discussed in Sec. II B. However, starting from rest, the fluid velocity cannot jump abruptly to a quasi-stationary distribution. For this reason, the time rate-of-change term $\partial u_z/\partial t$ in (7) cannot be omitted during the early stage of the recoil. The relevant momentum equation thus reads

$$\frac{\partial u_z}{\partial t} = -\frac{\gamma}{\rho}\frac{\partial \kappa}{\partial z} + 3\frac{\mu}{\rho \mathcal{R}^2}\frac{\partial}{\partial z}\left(\mathcal{R}^2 \frac{\partial u_z}{\partial z}\right). \tag{17}$$

To determine the initial evolution of the tip velocity, we follow the approach pioneered by Savva and Bush [8] for a retracting planar sheet. To this end, several assumptions are required. (*i*) The initial filament is made of a long cylindrical column with a hemispherical end; (*ii*) the filament may be considered as infinitely long, and its radius remains uniform and constant during the initial stage of the recoil; (*iii*) the velocity in the hemispherical blob is uniform. (*iv*) Last, the filament is set in motion by the $1/\mathcal{R}_0$ discontinuity in the mean curvature at the matching point between the hemispherical end and the cylindrical column, and this discontinuity persists throughout the initial stage. Equation (17) then reduces to

$$\frac{\partial u_z}{\partial t} = -\frac{\gamma}{\rho \mathcal{R}_0}\delta(z) + 3\frac{\mu}{\rho}\frac{\partial^2 u_z}{\partial z^2}, \tag{18}$$

where δ is the Dirac delta function resulting from the discontinuity of the mean curvature, and we provisionally consider that the origin of the z-axis is shifted to the position at which the column connects to the hemispherical end. Integrating (18) from $z = -\varepsilon$ to $z = +\varepsilon$ and considering the limit $\varepsilon \to 0$ yields

$$\frac{\partial u_z}{\partial z}(z = 0^-, t) = -\frac{1}{3}\frac{\gamma}{\mu \mathcal{R}_0}. \tag{19}$$

Hence, for $z \leq 0$, *i.e.* within the cylindrical column, (17) reduces to

$$\frac{\partial u_z}{\partial t} = 3\frac{\mu}{\rho}\frac{\partial^2 u_z}{\partial z^2}. \tag{20}$$

This governing equation is subject to (19) for $z \rightarrow= 0^-$, to the boundary condition $u_z(z,t) \rightarrow 0$ for $z \rightarrow -\infty$ (as the fluid is still at rest far from the discontinuity), and to the initial condition $u_z(z,0) = 0$ for all $z < 0$. Since the filament is considered infinitely long, its radius $\mathcal{R}_0$ is the only geometrical length scale left in the above problem. Therefore, the time scale involved in the heat equation (20) is the diffusive time $t_d = \rho \mathcal{R}_0^2/\mu = t_i^2/t_v$ characterizing viscous diffusion at the scale of the filament cross section, with $t_v = (\mu/\gamma)\mathcal{R}_0$ the characteristic viscous-capillary time defined in Sec. II B. Since surface tension only appears in the boundary condition (19), t_d is a purely diffusive time scale. The solution of the above problem reads [33]

$$\frac{u_z}{U_v} = \frac{2}{\sqrt{3\pi}}\sqrt{\frac{t}{t_d}}\exp\left(-\frac{z^2/\mathcal{R}_0^2}{12t/t_d}\right) + \frac{z/\mathcal{R}_0}{3}\text{erfc}\left(\frac{-z/\mathcal{R}_0}{2\sqrt{3t/t_d}}\right), \tag{21}$$

with $U_v = \gamma/\mu$. Thus the tip velocity $U_t = u_z(z = 0^-, t)$ evolves as

$$\frac{U_t}{U_v} = \frac{2}{\sqrt{3\pi}}\sqrt{\frac{t}{t_d}}. \tag{22}$$

The tip velocity still scales linearly with surface tension but is now inversely proportional to the square root of the fluid viscosity.
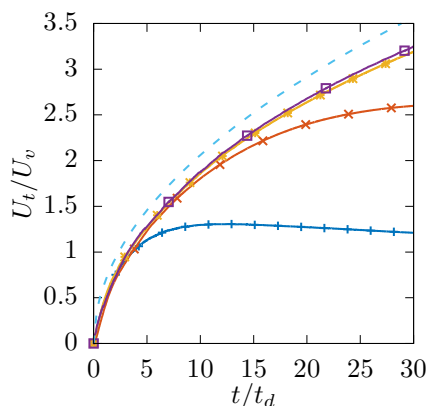

FIG. 11: Tip velocity *vs.* time for Oh $= 10$ and different initial aspect ratios during the initial transient. $-+-$: $\mathcal{A} = 5$, $-\times-$: $\mathcal{A} = 10$, $-*-$: $\mathcal{A} = 20$, $-\square-$: $\mathcal{A} = 40$, $--$: prediction (22).

Figure 11 displays the evolution of the tip velocity in the early stages of the recoil. For $0 \leq t/t_d \lesssim 5$, all curves collapse on the same master curve which is accurately predicted by (22). In contrast, for $t/t_d \gtrsim 5$, an increasing departure from the theory is observed for the shortest filament ($\mathcal{A} = 5$), the tip velocity of which weakly decreases over time beyond $t/t_d \gtrsim 12$. With $\mathcal{A} = 10$, the evolution of the tip velocity departs from (22) only for $t/t_d \gtrsim 15$, while no significant departure is observed for the largest two aspect ratios over the time window shown in the figure. These observations may be rationalized by coming back to (17) and considering that the filament has actually a finite length. In this case, the time rate-of-change term is of the same order as the viscous term up to a time of $\mathcal{O}(\mathcal{A}^2 t_d)$ after the recoil starts. Therefore, the longer the filament the larger the time period over which (22) holds, as Fig. 11 confirms.

C. Long-time behavior for Oh $\gg 1$

Figure 12 displays the evolution of the tip velocity throughout the recoil. Following the analysis performed in Sec. II B, the velocity is normalized by the viscous-capillary scale $\mathcal{A}U_v$. Similar to what was observed with Oh $= 1$, the tip velocity reaches a maximum, say U_{tm}, after the initial transient examined above. However, no plateau is observed here. Instead, the tip velocity starts to decrease just after the maximum is reached. Keeping in mind that $\mathcal{A}U_v/U_i = \mathcal{A}/Oh$, it turns out that U_{tm} ranges from $\approx 0.65U_i$ for the longest filament to $\approx 0.14U_i$ for the shortest one. Hence U_{tm} is much lower than the Taylor-Culick prediction in all cases. For short enough filaments, the recoil is already quasi-steady by the time the maximum is reached. In such cases, U_{tm} scales as $\mathcal{A}U_v$, in line with the conclusions of the dimensional analysis. In contrast, $U_{tm}/(\mathcal{A}U_v)$ is found to decrease significantly with $\mathcal{A}$ for the
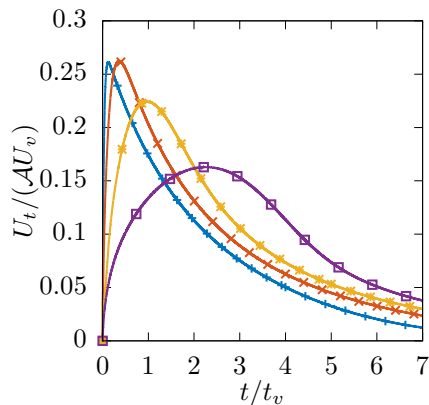
FIG. 12: Tip velocity *vs.* time for Oh = 10 and different initial aspect ratios. . $-+-$: $\mathcal{A} = 5$, $- \times -$: $\mathcal{A} = 10$, $- * -$: $\mathcal{A} = 20$, $-\square-$: $\mathcal{A} = 40$.

longest two filaments, an indication that the corresponding stage is not governed by a pure viscous-capillary balance. In other words, inertia is still important at this stage of the evolution of sufficiently long filaments. This is in line with the scaling analysis performed on (7), which led to the conclusion that inertia can only be neglected provided Oh $\gg \mathcal{A}$. A direct consequence of this limitation of the pure viscous-capillary balance is that U_{tm} cannot grow linearly with $\mathcal{A}$ for long enough filaments. Instead, the larger the aspect ratio the stronger the influence of fluid inertia. Therefore, for a given Oh and filaments such that $\mathcal{A}/Oh$ is not small, the longer the filament the closer the maximum tip velocity is to the Taylor-Culick prediction. Here for instance, U_{tm}/U_i increases from ≈ 0.45 for $\mathcal{A} = 20$ to 0.65 for $\mathcal{A} = 40$.
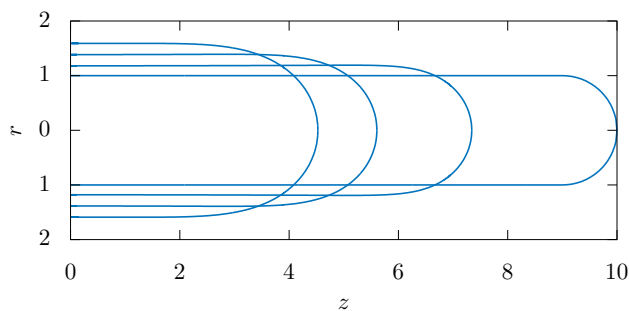

FIG. 13: Successive shapes of a retracting filament with Oh = 10 and $\mathcal{A} = 10$ (assuming $\mathcal{R}_0 = 1$). The time step between two successive snapshots is $\Delta t = 1.2 t_v$.

Figure 13 displays successive snapshots of the filament surface for an initial aspect ratio $\mathcal{A} = 10$. The initial shape made of a cylindrical column with a hemispherical end is found to survive throughout the 'life' of the filament, suggesting a self-similar evolution. In problems dominated by a viscous-capillary balance, the relevant similarity variables are [34, 35]

$$\eta = -\frac{z}{\frac{\gamma}{\mu}(t + t_0)}, \quad u_z(\eta) = \frac{\gamma}{\mu}U(\eta), \quad \mathcal{R}(\eta, t) = \frac{\gamma}{\mu}(t + t_0)R(\eta), \tag{23}$$

where it is assumed that $z = 0$ corresponds to the tip position and t_0 is the time shift required to ensure that $\mathcal{R}(z, t = 0) = \mathcal{R}_0$ far from the tip, *i.e.* for $\eta \to \infty$. Inserting the above definitions into the mass and momentum governing equations yields a coupled set of differential equations. Although no closed-form solution can be obtained, it may be shown that, to leading order, $R(\eta) \to 1/6$ for $\eta \to \infty$ [34]. Therefore (23) predicts that, far from the tip, the filament radius evolves as

$$\mathcal{R}(\eta \to \infty, t) = \frac{\gamma}{\mu}\frac{(t + t_0)}{6} = \mathcal{R}_0 \left(1 + \frac{1}{6}\frac{t}{t_v}\right). \tag{24}$$

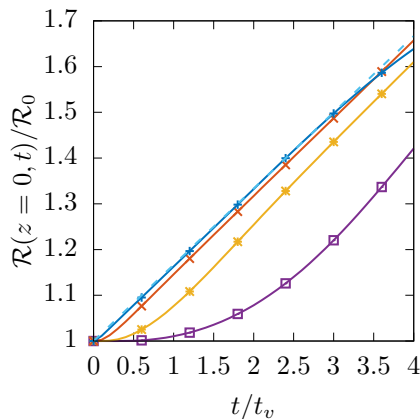FIG. 14: Evolution of the filament radius in the midplane $z = 0$ for Oh $= 10$. $-+-$: $\mathcal{A} = 5$, $-\times-$: $\mathcal{A} = 10$, $-*-$: $\mathcal{A} = 20$, $-\square-$: $\mathcal{A} = 40$, $--$: theoretical prediction (24).

Figure 14 shows how this prediction compares with the numerical evolution observed in the midplane $z = 0$. After an initial transient, the duration of which is only significant for the longest two filaments, the radius of the column is found to increase linearly in time. The corresponding slope closely follows the theoretical prediction (24). Assuming that the blob remains hemispherical and making use of the conservation of the filament volume $2\pi\mathcal{R}^2(\mathcal{L}-\mathcal{R})+4/3\pi\mathcal{R}^3$, the tip velocity (here equal to the blob velocity) is found to be

$$\frac{d\mathcal{L}}{dt} = \frac{U_v}{3}\left(\frac{1}{6} - \frac{\mathcal{A} - 1/3}{(1 + t/(6t_v))^3}\right) . \tag{25}$$

Therefore, with $U_t = -d\mathcal{L}/dt$, (25) predicts $U_t/U_v \to \mathcal{A}/3$ for $t/t_v \ll 1$, and $U_t/U_v \to 72\mathcal{A}(t_v/t)^3$ for $t/t_v \gg 1$, assuming $\mathcal{A} \gg 1$ in both cases.

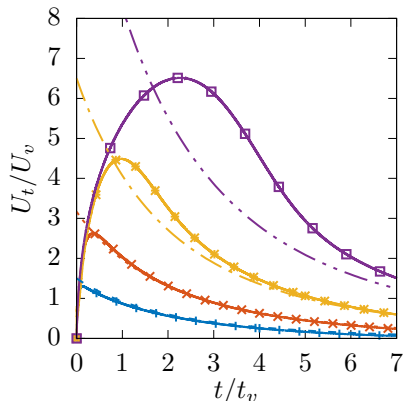FIG. 15: Evolution of the tip velocity for Oh $= 10$. $-+-$: $\mathcal{A} = 5$, $-\times-$: $\mathcal{A} = 10$, $-*-$: $\mathcal{A} = 20$, $-\square-$: $\mathcal{A} = 40$; dotted lines: theoretical prediction (25).

Figure 15 compares the numerical evolutions of the tip velocity obtained for the four initial aspect ratios with the prediction (25). The agreement is excellent for the shortest two filaments, including the estimate of the maximum velocity, which corresponds to the short-time limit of (25). The agreement deteriorates as the aspect ratio increases. The larger $\mathcal{A}$ the longer it takes for the tip velocity to follow the above viscous-capillary prediction, a direct effect of the persistence of significant inertial effects for long filaments that do not satisfy the condition Oh $\gg \mathcal{A}$.

V. SUMMARY AND CONCLUDING REMARKS

Using fully-resolved numerical simulations, we examined the evolution of the tip velocity $U_t(t)$ of a capillary-driven retracting viscous filament over a wide range of values of the Ohnesorge number, *i.e.* of the relative magnitude of

viscous and capillary effects. For small Oh-values, no matter what the initial aspect ratio of the filament is, the Taylor-Culick prediction matches the tip velocity observed beyond the initial acceleration stage pretty well. Only a slight overestimate is noticed, mainly because the velocity within the blob is nonuniform, which contradicts one of the assumptions involved in the Taylor-Culick model. Still at low Oh, oscillations of the tip velocity are observed throughout the recoil process. A simple mass-spring model considering how a change in the blob radius modifies the blob inertia and the capillary restoring force allows the period of these oscillations to be quantitatively predicted. These oscillations trigger the formation of capillary waves which form and propagate slightly faster than the tip at the surface of filaments with a sufficiently large aspect ratio. The final stage of the recoil is characterized by damped oscillations of the filament surface as it relaxes toward its equilibrium spherical shape. Beyond the initial period of their existence, during which their amplitude is large, these oscillations are found to obey predictions of the linear theory corresponding to the fundamental $l = 2$ mode.

For Oh $= \mathcal{O}(1)$, viscous effects significantly delay the retraction process. The initial acceleration stage lasts for a longer time than in the low-Oh regime, and the larger $\mathcal{A}$ the longer the duration of this first stage. Then the evolution of the tip velocity dramatically depends on the filament aspect ratio. For 'short' filaments, say $\mathcal{A} \lesssim 10$, U_t reaches a maximum significantly lower than the Taylor-Culick value, before decreasing monotonically to zero. In contrast, the tip velocity of 'long' filaments such that $\mathcal{A} \gtrsim 20$ reaches a plateau close to the Taylor-Culick prediction, before decreasing to zero after having changed its sign. This single change of sign during the final stage of the recoil is what is left of the damped oscillations observed during the same period in the low-Oh regime. The filament evolution becomes strikingly different when the Ohnesorge number is made one order of magnitude larger. In this regime, no blob forms and the filament radius grows almost uniformly as the recoil goes on. For short enough filaments, the tip velocity obeys a viscous-capillary scaling and its maximum increases linearly with $\mathcal{A}$. In contrast, inertial effects remain significant during most stages of the recoil of long enough filaments such that $\mathcal{A}/Oh \gtrsim 1$. The dynamics of filaments governed by a viscous-capillary balance was shown to obey a self-similar evolution. The corresponding theoretical solution accurately predicts both the maximum of of the tip velocity (reached during the early stage) and the power law characterizing its decay in the long-time limit.

In real applications, the initial shape of the filament is more complex than the canonical cylindrical column+ hemispherical end geometry considered here [20]. Therefore one can question the generality of the results reported in the present study, as well as those of previous studies based on the same intial geometry. In the low-Oh regime, the evolutions of U_t discussed in Appendix A and Sec. III A show that the initial tip acceleration dramatically depends on the initial geometry and volume of the blob. However, the corresponding dynamics become virtually indistinguishable beyond a time period of the order of the inertia-capillary time scale. This makes the later stages of the evolution of the tip velocity, especially its gradual approach to the Taylor-Culick prediction, robust with respect to slight changes in the initial geometry. The recoil dynamics being essentially driven by inertia and capillary forces in the blob region, details of the boundary condition at the opposite end of the ligament do not matter. The situation is dramatically different when the Ohneorge number is large. In this regime, the self-similar nature of the evolution makes the initial geometry drive entirely the long-term shape of the filament. Moreover, viscous forces being of primary importance, this evolution is influenced by the boundary condition at the opposite end of the tip , *i.e.* by the elongational strain rate at the position at which the filament is held. This point is discussed in more detail in the companion paper [21] focused on a viscous retracting sheet.

Appendix A: Effect of the initial shape of the filament on the recoil process in the low-Oh regime

Tong and Wang [36] performed numerical simulations of retracting filaments with different initial end shapes. They observed an important influence of the end shape on the likelihood of the filament pinch-off. However, they did not investigate the corresponding potential effects on the tip velocity. With this objective in mind, we performed computations for several additional end shapes in the low-Oh regime. Here we focus on the case where the initial shape of the filament consists in a long cylindrical column ended with a prolate spheroid of half-length $2\mathcal{R}_0$ and radius $\mathcal{R}_0$. The initial aspect ratio of the filament is set to $\mathcal{A} = 20$. Thanks to this prolate spheroidal end, the transition from a mean curvature $\kappa = 1/\mathcal{R}_0$ along to column to a larger curvature at the tip is more gradual than in the case of a spherical end, for which κ jumps abruptly from $\kappa = 1/\mathcal{R}_0$ to $\kappa = 2/\mathcal{R}_0$.
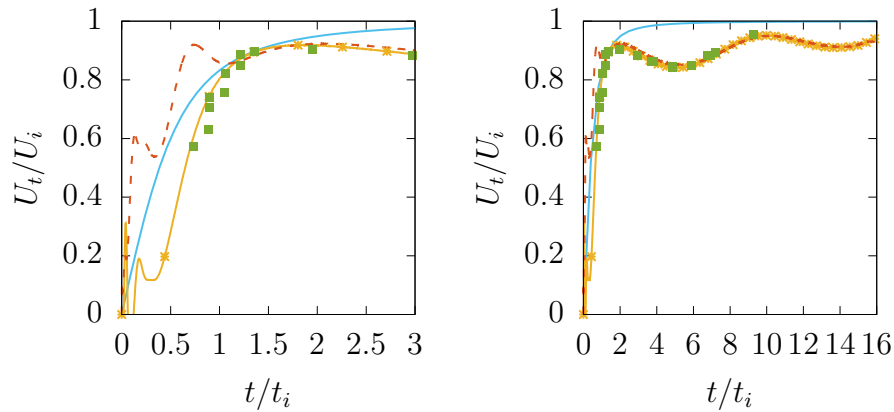
FIG. 16: Tip velocity versus time for Oh = 0.1 and $\mathcal{A} = 20$. (left): early stage stage of the recoil process; (right): intermediate stage. —— : prolate spheroidal end; — ∗ — : spherical end; — : prediction (10); ■ : numerical results from [10] for $\mathcal{A} = 15$.
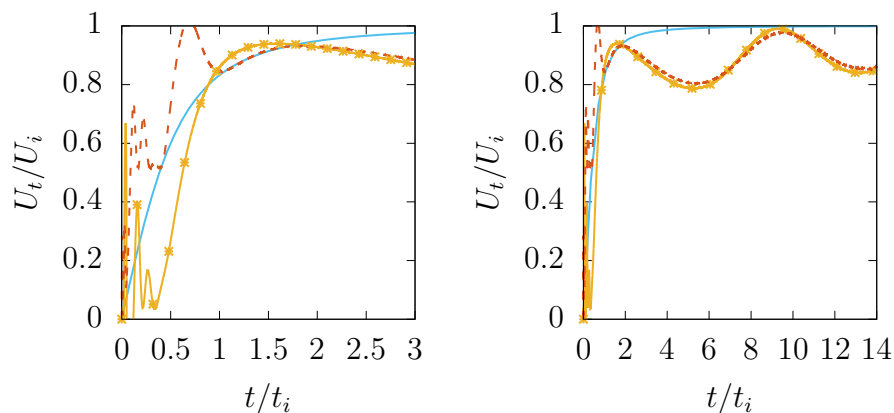

FIG. 17: Same as figure 16 for Oh = 0.05.

Figure 16 displays the evolution of the tip velocity for the two different initial end shapes in the case the Ohnesorge number is set to 0.1. The two evolutions exhibit large differences at the beginning of the recoil process, with a much sharper increase in the case of the prolate end. This is no surprise since the two distributions of the interface curvature in the tip region differ. Strong oscillations are observed with both geometries, due to the two sources of disturbances associated with the initial condition (see the discussion in Sec. III A). Nevertheless, both evolutions converge for $t \gtrsim t_i$ and only tiny differences subsist beyond $t \approx 1.2 t_i$.

To determine how much the above conclusions are influenced by small viscous effects, we repeated the above two computations with Oh = 0.05. The results are displayed in Fig. 17. Again, the initial shape is seen to play a major role during the initial stage of the recoil. The overshoots noticed in the tip velocity within this early period have a larger magnitude than those found with Oh = 0.1, a direct consequence of the weaker viscous damping resulting from the twice as small viscosity. Nevertheless, the two evolutions become very close to each other beyond $t/t_i \approx 1.7$, although some tiny differences in amplitude and phase remain at later times between the two series of oscillations. Therefore the critical time beyond which the initial geometry does not keep a significant influence on the filament dynamics is found to increase with $\mathrm{Oh}^{-1} = t_d/t_i$, where t_d is the diffusive time introduced in Sec. IV B. Not unlikely, this increase suggests that the dynamics of long filaments corresponding to very small values of Oh, say Oh = $\mathcal{O}(10^{-2})$ or less, may still be influenced by the initial shape over much longer periods of time. Since break-up is likely to occur through the end-pinching or capillary wave mechanisms at a quite early stage under such extreme conditions [12], there is little doubt that the corresponding dynamics remains influenced by the initial shape throughout the 'life' of the filament.

Coming back to the flow conditions considered in the present study, the results reported in Figs. 16 and 17 indicate that the dynamics observed beyond an $\mathcal{O}(t_i)$-long initial stage are robust with respect to the choice of the initial shape. This strengthens the validity of the reasoning underlying the Taylor-Culick prediction, as well as the physical

arguments used to explain the origin of the oscillations observed in the tip velocity.

[1] J. Eggers and E. Villermaux. Physics of liquid jets. *Rep. Prog. Phys.*, 71:036601, 2008.

[2] T. Driessen, R. Jeurissen, H. Wijshoff, F. Toschi, and D. Lohse. Stability of viscous long liquid filaments. *Phys. Fluids*, 25:062109, 2013.

[3] G. I. Taylor. The dynamics of thin sheets of fluid. III. Disintegration of fluid sheets. *Proc. R. Soc. London Ser. A*, 253: 313–321, 1959.

[4] F. E. C. Culick. Comments on a ruptured soap film. *J. Appl. Phys.*, 31:1128–1129, 1960.

[5] W. R. McEntee and K. J. Mysels. Bursting of soap films. i. an experimental study. *J. Phys. Chem.*, 73:3018–3028, 1969.

[6] M. P Brenner and D. Gueyffier. On the bursting of viscous films. *Phys. Fluids*, 11:737–739, 1999.

[7] G. Sünderhauf, H. Raszillier, and F. Durst. The retraction of the edge of a planar liquid sheet. *Phys. Fluids*, 14:198–208, 2002.

[8] N. Savva and J. W. M. Bush. Viscous sheet retraction. *J. Fluid Mech.*, 626:211–240, 2009.

[9] M. Murano and K. Okumura. Bursting dynamics of viscous film without circular symmetry: The effect of confinement. *Phys. Rev. Fluids*, 3:031601, 2018.

[10] P. K. Notz and O. A. Basaran. Dynamics and breakup of a contracting liquid filament. *J. Fluid Mech.*, 512:223–256, 2004.

[11] R. M. S. M. Schulkes. The contraction of liquid filaments. *J. Fluid Mech.*, 309:277–300, 1996.

[12] C. R. Anthony, P. M. Kamat, M. T. Harris, and O. A. Basaran. Dynamics of contracting filaments. *Phys. Rev. Fluids*, 4: 093601, 2019.

[13] H. A. Stone, B. J. Bentley, and L. G. Leal. An experimental study of transient effects in the breakup of viscous drops. *Journal of Fluid Mechanics*, 173:131–158, 1986.

[14] H. A. Stone. Dynamics of drop deformation and breakup in viscous fluids. *Annu. Rev. Fluid Mech.*, 26:65–102, 1994.

[15] F. Wang, F. P. Contò, N. Naz, J. R. Castrejón-Pita, A. A. Castrejón-Pita, C. G. Bailey, W. Wang, J. J. Feng, and Y. Sui. A fate-alternating transitional regime in contracting liquid filaments. *J. Fluid Mech.*, 860:640–653, 2019.

[16] J. Hoepffner and G. Paré. Recoil of a liquid filament: escape from pinch-off through creation of a vortex ring. *J. Fluid Mech.*, 734:183–197, 2013.

[17] J. B. Keller. Breaking of liquid films and threads. *Phys. Fluids*, 26:3451–3453, 1983.

[18] J. L. Pierson and J. Magnaudet. Inertial settling of a sphere through an interface. Part 2. Sphere and tail dynamics. *J. Fluid Mech.*, 835:808–851, 2018.

[19] F. P. Contò, J. F. Marín, A. Antkowiak, J. R. Castrejón-Pita, and L. Gordillo. Shape of a recoiling liquid filament. *Sci. Rep.*, 9:1–8, 2019.

[20] C. Planchette, F. Marangon, W. K. Hsiao, and G. Brenn. Breakup of asymmetric liquid ligaments. *Phys. Rev. Fluids*, 4: 124004, 2019.

[21] H. Deka and J. L. Pierson. Revisiting the Taylor-Culick approximation. Part 2 : retraction of a viscous sheet (submitted). 2020.

[22] J. Eggers and T. F. Dupont. Drop formation in a one-dimensional approximation of the Navier–Stokes equation. *J. Fluid Mech.*, 262:205–221, 1994.

[23] M. Song and G. Tryggvason. The formation of thick borders on an initially stationary fluid sheet. *Phys. Fluids*, 11: 2487–2493, 1999.

[24] L. Gordillo, G. Agbaglah, L. Duchemin, and C. Josserand. Asymptotic behavior of a retracting two-dimensional fluid sheet. *Phys. Fluids*, 23:122101, 2011.

[25] S. Popinet. A quadtree-adaptive multigrid solver for the Serre–Green–Naghdi equations. *J. Comput. Phys.*, 302:336–358, 2015.

[26] S. Popinet. An accurate adaptive solver for surface-tension-driven interfacial flows. *J. Comput. Phys.*, 228:5838–5866, 2009.

[27] J. B. Bell, P. Colella, and H. M. Glaz. A second-order projection method for the incompressible Navier-Stokes equations. *J. Comput. Phys.*, 85:257–283, 1989.

[28] S. Popinet. Numerical models of surface tension. *Annu. Rev. Fluid Mech.*, 50:49–75, 2018.

[29] J. L. Pierson. *Basilisk script*, 2019. http://basilisk.fr/sandbox/piersonj/.

[30] G. K. Batchelor. *An Introduction to Fluid Dynamics.* Cambridge Univ. Press, 1967.

[31] S. Chandrasekar. *Hydrodynamic and Hydromagnetic Stability.* Oxford Univ. Press, 1961.

[32] H. Lamb. *Hydrodynamics (6th ed.).* Cambridge Univ. Press, 1945.

[33] H. S. Carslaw and J. C. Jaeger. *Conduction of Heat in Solids.* Oxford Univ. Press, 1959.

[34] J. Eggers. Post-breakup solutions of Navier-Stokes and Stokes threads. *Phys. Fluids*, 26:072104, 2014.

[35] J. Eggers and M. A. Fontelos. *Singularities: Formation, Structure, and Propagation.* Cambridge Univ. Press, 2015.

[36] A. Y. Tong and Z. Wang. Relaxation dynamics of a free elongated liquid ligament. *Phys. Fluids*, 19:092101, 2007.